

UCLA

UCLA Previously Published Works

Title

Non-muscle myosin II inhibition at the site of axon injury increases axon regeneration.

Permalink

<https://escholarship.org/uc/item/9z97k7qx>

Journal

Nature Communications, 16(1)

Authors

Heo, Keunjung

Ho, Tammy

Zeng, Xiangsunze

et al.

Publication Date

2025-03-26

DOI

10.1038/s41467-025-58303-6

Peer reviewed

Non-muscle myosin II inhibition at the site of axon injury increases axon regeneration

Received: 14 August 2024

Accepted: 14 March 2025

Published online: 26 March 2025

 Check for updates

Keunjung Heo^{1,2,7}, Tammy Szu-Yu Ho^{1,2,7}, Xiangsunze Zeng^{1,2},
Bruna Lenfers Turnes^{1,2}, Maryam Arab^{1,2}, Selwyn Jayakar^{1,2}, Kuchuan Chen^{1,2},
Georgios Kimourtzis^{1,2}, Michael C. Condro³, Elisa Fazzari⁴, Xuan Song^{1,5},
J. Tabitha Hees¹, Zhuqiu Xu^{1,2}, Xirui Chen^{1,2}, Lee B. Barrett^{1,2}, Laura Perrault¹,
Roshan Pandey^{1,2}, Kathleen Zhang¹, Aparna Bhaduri⁴, Zhigang He^{1,5},
Harley I. Kornblum³, Jed Hubbs⁶ & Clifford J. Woolf^{1,2} ✉

Motor axon regeneration following peripheral nerve injury is critical for motor recovery but therapeutic interventions enhancing this are not available. We conduct a phenotypic screen on human motor neurons and identified blebbistatin, a non-muscle myosin II inhibitor, as the most effective neurite outgrowth promotor. Despite its efficacy *in vitro*, its poor bioavailability limits *in vivo* application. We, therefore, utilize a blebbistatin analog, NMII2, to explore its therapeutic potential for promoting axon regeneration. Local NMII2 application directly to injured axons enhances regeneration in human motor neurons. Furthermore, following a sciatic nerve crush injury in male mice, local NMII2 administration to the axonal injury site facilitates motor neuron regeneration, muscle reinnervation, and functional recovery. NMII2 also promotes axon regeneration in sensory, cortical, and retinal ganglion neurons. These findings highlight the therapeutic potential of topical NMII inhibition for treating axon damage.

Injuries to both the central nervous system (CNS) and peripheral nervous system (PNS) affect millions of individuals and are devastating, but there are no approved drugs to either induce the regeneration of injured CNS neurons or accelerate regeneration in the PNS. Lower motor neurons, which reside in the spinal cord and extend axons to innervate skeletal muscles, are highly susceptible to peripheral nerve injury, the prevalence of which is increasing¹. After a traumatic nerve injury, mature motor neurons only regenerate at a rate of 1–4 mm per day, the slowness of which results in only ~45% of injured axons achieving anatomical reinnervation of their muscle targets with, in consequence, limited functional recovery^{1–7}. Discovering therapeutic targets for effective treatment of axon injury is therefore critical to ensure a more complete recovery of motor and other disturbed

functions. Here, we show administration of a non-muscle myosin II inhibitor directly to an injured peripheral nerve increases motor axon regeneration.

To identify potential drug-based therapies for promoting axon regeneration, we established a high-throughput screening funnel capable of identifying targets that promote axon regeneration in human induced pluripotent stem cell (iPSC)-derived motor neurons. We screened 4557 bioactive compounds and identified blebbistatin, a non-muscle myosin II (NMII) inhibitor, as the most effective compound for promoting neurite outgrowth in motor neurons. NMII is a motor protein controlling actin arch formation and microtubule dynamics^{8–13}. Structurally, the globular head domain of NMII contains actin-binding regions and enzymatic Mg²⁺-ATPase motor domains^{14,15}. When

¹F.M. Kirby Neurobiology Center, Boston Children's Hospital, Boston, MA, USA. ²Department of Neurobiology, Harvard Medical School, Boston, MA, USA. ³Intellectual and Developmental Disabilities Research Center and the Departments of Psychiatry, Pharmacology and Pediatrics, University of California, Los Angeles, CA, USA. ⁴Department of Biological Chemistry, University of California, Los Angeles, CA, USA. ⁵Department of Neurology and Ophthalmology, Harvard Medical School, Boston, MA, USA. ⁶Rosamund Stone Zander Translational Neuroscience Center, Boston Children's Hospital, Harvard Medical School, Boston, MA, USA. ⁷These authors contributed equally: Keunjung Heo, Tammy Szu-Yu Ho. ✉e-mail: Clifford.Woolf@childrens.harvard.edu

regulatory light chains (RLCs) from the head domain of NMII are phosphorylated, NMII unfolds¹⁴, and upon binding to actin, the ATPase activity of the head induces a conformational change that moves actin filaments in an anti-parallel manner, enhancing contractility^{14,16–22}. In neurons, NMII binds to actin rings, exerting a contractile force that squeezes the actin ring inward and consequently keeps microtubule bundles tight, stabilizing the bundles within axons^{9,23}. In the growth cone, NMII increases actomyosin contractility, physically blocking microtubules, which results in only a few dynamic microtubules being present at the tip of the growth cone^{9,23}.

The identification of NMII as a target in our screen, together with its known biological actions, suggests that NMII inhibition may be a promising therapeutic strategy to promote axon regeneration. We find that its actions are not restricted to motor axons or the PNS, as NMII inhibition also enhances axon growth in mouse dorsal root ganglion (DRG) neurons and retinal ganglion cells (RGCs), and in human cortical neurons^{24–26}. Blebbistatin is an efficacious NMII inhibitor *in vitro*, but its poor bioavailability and photosensitivity limit its application *in vivo*²⁷. While blebbistatin and some of its analogs have been shown before to promote neurite outgrowth,^{24,26,28} local effects on axonal injury were not investigated.

We utilized a potent and stable blebbistatin analog²⁹, NMIIi2, to evaluate the therapeutic potential of NMII inhibition for increasing regeneration. Local application of NMIIi2 to injured axons promotes axonal growth *in vitro*, and direct NMIIi2 application to an injured nerve *in vivo* accelerates motor and sensory axon regeneration and functional recovery, underscoring topical application as a potential therapeutic intervention for axon injury.

Results

A phenotypic screen for pro-regenerative compounds in human motor neurons

To identify compounds that promote axon regeneration, we first performed a primary screen using 4 bioactive compound libraries (Mechanism of Action, Selleck Bioactive, Biomol collection, and Prestwick 3 collection) on a phenotypic axon growth assay in human iPSC-derived motor neurons (Fig. 1A and B). The top 10 compounds promoting neurite outgrowth from the primary screen were then evaluated for dose-response characteristics, and the compounds' effects on motor axon injury examined using a spot culture that allows for evaluation of drug action on axon outgrowth after axonal injury (Fig. 1B). To confirm that the observed effects were not cell line-specific and representative of human motor neurons across diverse genetic and demographic backgrounds, we performed primary and secondary screens using three different human cell lines of mixed gender. The most promising target was then independently validated using short hairpin RNA (shRNA), and efficacy in promoting functional recovery evaluated in a mouse model of sciatic nerve crush injury.

For the primary screen, human iPSCs were differentiated into motor neurons (MNs) using an established protocol³⁰. On day 14 of the MN differentiation, approximately 8000 neurons per well were replated, on a 96-well plate coated with chondroitin sulfate proteoglycan (CSPG), including neurocan, phosphacan, versican, and aggrecan, to create a non-growth permissive environment (Fig. 1C). Neurite growth was significantly inhibited in neurons grown on the CSPG substrate compared to laminin-coated plates (Fig. 1C and D), replicating the axon growth inhibitory characteristics of the CNS. The compounds were added to the culture on the same day the neurons were seeded on the plate and incubated for 24 h. For quantification of neurite length, the neurons were imaged and analyzed using an ArrayScan XTI imaging platform (Fig. 1B) after fixation and staining with antibodies against TUBB3 (Fig. 1C). The ROCK inhibitor Y-27632, which promotes regeneration after nerve injury^{31,32}, was used as positive control (Supplementary Fig. S1A) and DMSO as a negative control (Supplementary Fig. S1A).

Using this platform, we screened 4557 bioactive compounds with diverse structures and targets, including ion channels, proteases, and kinases, and identified the 10 compounds that promoted maximal motor neuron neurite outgrowth in the non-permissive CSPG environment: blebbistatin, RKI-1447, Fasudil, CEP-33779, Y-27632, thiazovivin, momelotinib, CCT128930, benidipine hydrochloride and AT7867 (Fig. 1E). These ten compounds were then subjected to a dose-response evaluation to identify optimal concentrations (Supplementary Fig. S1B–S1H). We then monitored neurite outgrowth for each compound at its optimal dose level over a 5-day period using an IncuCyte S3 Live-Cell Analysis System (Fig. 1F and G). Blebbistatin again emerged as the most potent neurite outgrowth-promoting compound on the CSPG (Fig. 1F and G). We also examined the effects of the top 5 compounds directly on axon regeneration by applying a laser cut injury to axons, using spot cultures, which align the cell bodies in the center with their axons projecting peripherally in a radial fashion (Supplementary Fig. S2A, S2B, and S2G). Again, blebbistatin was the most potent compound for directly promoting axonal regeneration after a clearly defined axonal injury (Supplementary Fig. S2C–S2F, and S2H), and therefore, it was selected for a more detailed assessment.

To provide additional insight into the safety profile of the screened compounds, we evaluated cell viability following treatment with the nine top compounds identified in the screen, using a viability/cytotoxicity assay with Calcein-AM and ethidium homodimer-1 (EthD-1) dyes, as previously described³³. Treatment with blebbistatin, our lead compound, neither changed cell viability nor induced cytotoxicity (Supplementary Fig. SII–K). However, cells treated with the two ROCK1/ROCK2 inhibitors (Fasudil and Y27632), a JAK2 inhibitor (CEP-33779), or a voltage-gated calcium channel blocker (Benidipine-HCl) all exhibited reduced EthD-1 intensity (Supplementary Fig. SIK), suggesting that while these compounds promote neurite outgrowth at the tested concentrations, they may also modify cell survival.

A blebbistatin analog also promotes axonal regeneration

Although blebbistatin promotes neurite outgrowth *in vitro*, its limited bioavailability and high photosensitivity restrict its application *in vivo*^{27,34}. To overcome these limitations, we synthesized an analog of blebbistatin²⁹, which we term NMIIi2 (Supplementary Fig. S3A). NMIIi2 exhibits higher photostability, greater selectivity for NMII, and reduced selectivity for cardiac myosin II compared to blebbistatin²⁹. Through dose-response analyses, we identified the most efficacious concentrations for promoting neurite outgrowth as 10 μ M for NMIIi2 and 25 μ M for blebbistatin (Supplementary Fig. S3B and S3C). Treatment with either blebbistatin or NMIIi2 facilitated significant axonal extension of motor neurons on CSPG at 24 h, with sustained effects up to 72 h post-treatment (Fig. 2A and C). The addition of these NMII inhibitors to motor neurons on a growth-permissive substrate (laminin) led to maximal neurite growth within the initial 24 h period, followed by a growth rate similar to vehicle-treated neurons at 48 and 72 h (Fig. 2B and D).

Interestingly, the axonal growth *in vitro* also included increased branch formation (Fig. 2B). To further examine this, we analyzed the total number of branch points, normalized to TUBB3-labeled neuronal counts per field, after treatment with the two NMII inhibitors (Fig. 2E–H). Under non-permissive growth conditions (CSPG), the addition of NMIIi2 or blebbistatin increased branch points by 368% and 280% per neuron, respectively (Fig. 2E and G). In the growth permissive condition (laminin), NMIIi2 or blebbistatin treatment led to an increase in branch points of 134% and 83.0% per neuron (Fig. 2F and H). NMIIi2 and blebbistatin exposure to motor neurons *in vitro* induces, therefore, both axonal elongation and increased branching in both non-permissive and permissive growth conditions.

Next, we assessed the effect of NMIIi2 on axon regeneration in motor neuron spot cultures grown on laminin (Fig. 3A). We applied a laser-cut injury ~200 μ m from the edge of cell body cluster (proximal

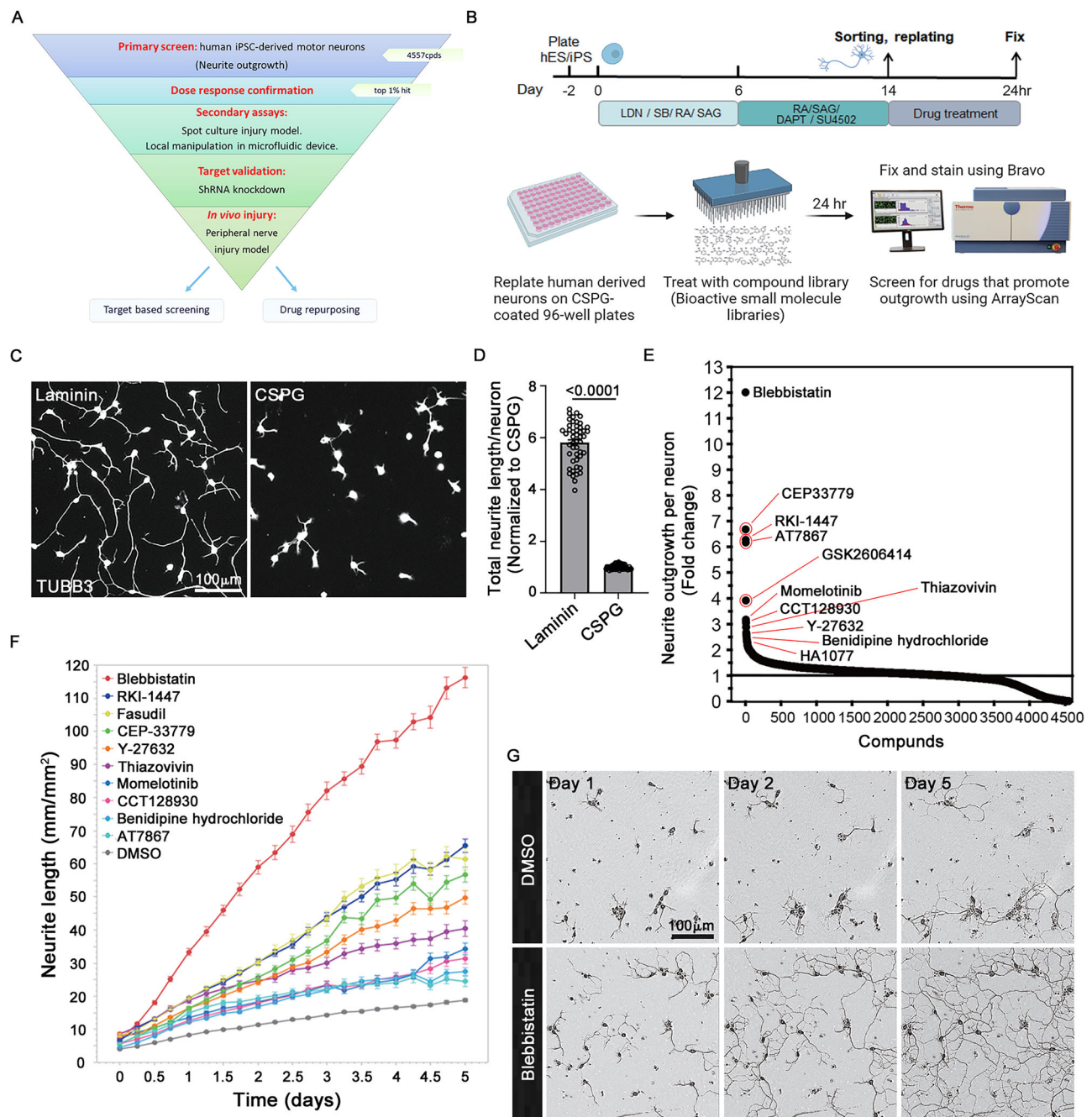
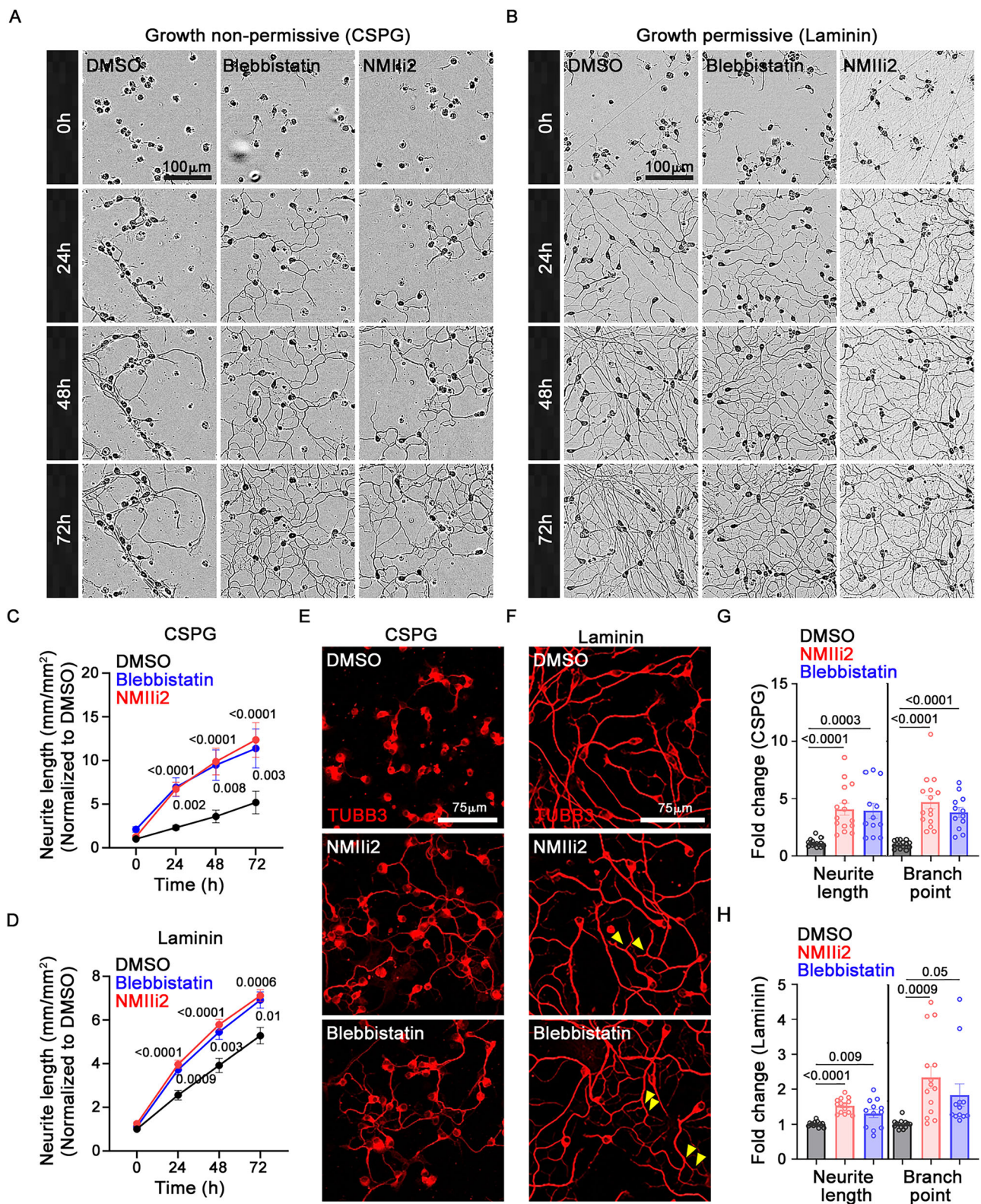


Fig. 1 | High-throughput phenotypic screening platform with human iPSC-derived motor neurons to identify pro-regenerative compounds. Screening funnel illustrating the screening strategy (A), and a schematic of the primary compound screen strategy (B), illustrated by BioRender. Zeng, X. (2025) <https://BioRender.com/f56i717>. Human iPSC-derived MNs, after replating in 96 well plates, were cultured for 24 h on laminin or CSPG and stained with an antibody against TUBB3 (C). Quantification of total neurite length per neuron on the growth substrates, normalized to CSPG (D). Experiments were done in two biological replicates and analyzed from 48 technical replicates per group. Statistics, unpaired two-tailed *t* test, SEM error bars, and *p*-value: <math>< 0.0001</math>. Data is available in the Source

Data file. Primary screen of 4557 bioactive compounds (E). Each dot represents a single compound, and the black line indicates a fold change of 1. The top 10 candidates promoting neurite outgrowth are identified. F Quantification of neurite length (mm/mm²) after incubation with the 10 compounds: 25 μM blebbistatin, 15 μM RKI-1447, 10 μM Fasudil, 10 μM CEP-33779, 20 μM Y-27632, 50 μM thiazovivin, 10 μM momelotinib, 10 μM CCT128930, 10 μM benidipine hydrochloride, and 10 μM AT7867. Images captured every 6 h for 5 days. Data presented as mean ± SEM, experiments were done in three replicates. G Live cell images of neurons at days 1, 2, and 5 with DMSO or 25 μM blebbistatin incubation.

site injury) or ~700 μm from the cell body cluster, near the axon terminals (distal site injury) (Fig. 3A). The proximal site injury affects both dendrites and axons, whereas the distal site injury acts primarily on axons. Post-injury, the neurons were incubated with DMSO or NMII2 and monitored every 4 h for 24 h to assess the regeneration response. Because it is technically difficult to identify and measure

total neurite length in spot cultures, we used an automated SNT script which cropped the injury site to a consistent size, adjusted the threshold, and binarized the images (Fig. 3A). Axon density distal to the injury site increased by 123% per neuron at 12 h and continued to increase by 144% 24 h post NMII2 treatment compared to DMSO after a proximal site injury (Fig. 3B and D). Axon density increased by



121% at 12 h and 142% at 24 h after a distal site injury post NMIIi2 incubation (Fig. 3C and E). These results indicate again that NMIIi2 treatment promotes axonal growth and branching after axonal injury. Injured motor neurons treated with NMIIi2 exhibit a growth phenotype similar to blebbistatin, although at a lower concentration, and, therefore, we then decided to use NMIIi2 to characterize the consequences of NMII inhibition and determine exactly where it is acting.

Local treatment of injured axons with NMIIi2 promotes regeneration

To investigate if local NMII inhibition in injured axons promotes regeneration, we cultured the human motor neurons in a microfluidic chamber enabling spatial segregation of the cell bodies/proximal axons and distal axons. Following an axotomy of the distal axons, we applied NMIIi2 to one of the two chambers using volumetric gradient flow and measured total axon length and branch points 24 h post-

Fig. 2 | NMII inhibition enhances neurite growth and branching. Representative images of neurons cultured on CSPG (A) or laminin (B) 24, 48, and 72 h post incubation with DMSO, 25 μ M blebbistatin, or 10 μ M NMIIi2. Scale bar: 100 μ m. Quantification of neurite length (mm/mm²) on CSPG (C) or laminin (D) substrates. Experiments performed in biological triplicates. Spot counts: 13 DMSO, 13 NMIIi2, and 12 blebbistatin on CSPG (C), and 12 DMSO, 12 NMIIi2, and 11 blebbistatin on laminin (D). Neurite length normalized to DMSO at 0 h. Statistical measurement two-way ANOVA with Tukey's *post hoc* test, SEM error bars. Sample number and *p*-values as follows: CSPG - At 0 h: NMIIi2 (*n* = 13), Blebbistatin (*n* = 12). At 24 h: NMIIi2 (*n* = 13; *p* < 0.0001), Blebbistatin (*n* = 12; *p* = 0.002). At 48 h: NMIIi2 (*n* = 13; *p* < 0.0001), Blebbistatin (*n* = 12; *p* = 0.003). At 72 h: NMIIi2 (*n* = 13; *p* < 0.0001), Blebbistatin (*n* = 12; *p* = 0.008). Laminin - At 0 h: NMIIi2 (*n* = 12), Blebbistatin (*n* = 11). At 24 h: NMIIi2 (*n* = 12; *p* < 0.0001), Blebbistatin (*n* = 11; *p* = 0.0009). At 48 h:

NMIIi2 (*n* = 12; *p* < 0.0001), Blebbistatin (*n* = 11; *p* = 0.003). At 72 h: NMIIi2 (*n* = 12; *p* = 0.0006), Blebbistatin (*n* = 11; *p* = 0.01). Wells stained with an antibody against TUBB3 in CSPG (E) or laminin (F) after incubation with DMSO, 25 μ M blebbistatin, or 10 μ M NMIIi2. Scale bar: 75 μ m. The arrowhead indicates branch points (yellow). Experiments conducted in biological triplicates. Sample number: 15 DMSO, 15 NMIIi2, and 12 blebbistatin on CSPG (G), and 14 DMSO, 14 NMIIi2, and 12 blebbistatin on laminin (H). Neurite length and branch points were quantified per neuronal count per field and normalized to DMSO for each condition. Stats: nonparametric Kruskal–Wallis test with Dunn's multiple comparison test or two-sided Welch's test with Dunnett's multiple comparison test. SEM error bars are shown. *P*-values are indicated in the graph. Data for Fig. (C, D, G, and H) are available in the Source Data file.

treatment (Fig. 4A and B). While treatment of the cell body/proximal axon site with NMIIi2 increased total branch length and branch points in the distal axons, a significantly more pronounced effect was observed with local administration of NMIIi directly on the distal injured axons (Fig. 4C–E). Local NMIIi2 treatment at the site of axonal injury of adult mouse dorsal root ganglion (DRG) sensory neurons also induced significantly greater regrowth (Supplementary Fig. S4A and S4B). These results show that NMII inhibition at the site of an axotomy promotes axonal elongation and branching in motor and sensory neurons, implicating that NMII locally modulates myosin within axons or growth cones⁹ to slow axon regrowth.

NMIIi2 treatment also promotes neurite outgrowth in human iPSC-derived cortical-like neurons cultured both on CSPG (Supplementary Fig. S5A and S5B) and laminin substrates (Supplementary Fig. S5C and S5D), like the actions of NMII inhibition on motor neurons, and the treatment also increased axonal growth phenotypes in neurons derived from cortical organoids (Supplementary Fig. S5E, S5F, S5G and S5H). Furthermore, an increase in total neurite length was also observed in adult mouse dissociated retina ganglion cells 72 h following NMIIi2 treatment when grown on CSPG and laminin substrates (Supplementary Fig. S5I–S5K). Taken together, these results indicate that NMIIi2 promotes neurite outgrowth in CNS as well as PNS neurons.

MYH9 knockdown increases axon growth

MYH9 encodes the heavy chain of non-muscle myosin IIA, which plays a pivotal role in ATP hydrolysis upon myosin binding to actin^{14,16,17}. To validate that the increased axon regrowth by the two NMII inhibitors is specifically due to NMII inhibition, we knocked down MYH9 by introducing a MYH9 shRNA by lentiviral transduction and assessed the axonal growth response after 5 days. The knockdown efficiency of the MYH9 shRNA was verified by Western blot, revealing a 55% reduction in MYH9 levels in neurons transduced with MYH9 shRNA, compared to those with a scrambled shRNA (Supplementary Fig. S6A and S6B). Next, we labeled human motor neuron spot cultures with TUBB3 and F-actin antibodies and performed a Sholl analysis to assess axon arborization. Compared to the scrambled shRNA, the sum of intersections increased by 212% in neurons transfected with MYH9 shRNA (Supplementary Fig. S6C and S6D). We then assessed axon regeneration in spot cultures expressing MYH9 shRNA after a laser-induced axotomy (Supplementary Fig. S6E). Compared to scrambled shRNA, a 133% increase was present in neurons with MYH9 knockdown 24 h post-injury (Supplementary Fig. S6F). While we were unable to confirm a link between MYH9 knockdown and enhanced axonal growth using immunostaining, our results indicate that the increased axonal growth resulting from NMII inhibition likely is the consequence of the suppression of MYH9 activity.

Local administration of NMIIi2 to an injured peripheral nerve improves motor and sensory recovery in vivo

To assess the impact of NMII inhibition in vivo in mice, we applied NMIIi2 locally to the site of a sciatic nerve crush injury. The crush injury

model facilitates faster nerve regeneration than after a nerve transection, which typically results in little or no functional recovery⁷, enabling more rapid recovery of motor and sensory function. This makes the crush injury model a preferred choice for axon regeneration studies. This was done by encapsulating 100 μ M NMIIi2 in a silicon tube with collagen hydrogel to facilitate extended drug delivery, and the tube placed around the nerve at the site of the crush (Fig. 5A). We tracked the regeneration of motor axons in the sciatic nerve by labeling them with a myelinated axon marker, neurofilament (NF), and the motor neuron marker choline acetyltransferase (ChAT) (Supplementary Fig. S7A). Compared to vehicle treatment, NMIIi2-treated nerves showed a 156% increase in ChAT label in the nerve distal to the crush site on day 7 post-injury (Supplementary Fig. S7B). We then investigated the extent of reinnervation of lumbrical muscles in the hind paw post-sciatic nerve crush. Using the pre/post-synaptic markers NF, synaptophysin (SYP), and α -bungarotoxin (BTX), we quantified pre/post-synaptic co-localization in the muscle. By day 7, the nerves had not yet reached the muscle in either the vehicle or treatment group (Supplementary Fig. S8A and S8C). In naïve mice with intact sciatic nerves, pre- and post-synaptic co-localization was highly prominent in lumbrical muscles but decreased by 90% on day 14 post-sciatic nerve crush injury in vehicle-treated mice (Fig. 5B and C), indicating that very few motor axons, had recontacted the muscle at this time point. However, mice locally treated with NMIIi2 at the crush site showed a 50% increase in pre/post-synaptic co-localization on day 14 relative to the vehicle group (Fig. 5B and C). By day 28, when nerve regeneration was complete, pre- and post-synaptic colocalization in the muscle reached similar levels in NMIIi2-treated and non-injured conditions (Supplementary Fig. S8B and S8C), indicating that successful reinnervation occurred in vehicle-treated mice by day 28, two weeks later than the NMIIi2-treated mice.

To assess motor function recovery, we utilized a machine learning-based platform to assess hind paw surface contact by measuring changes in paw luminance using frustrated total internal reflection³⁵. The paw luminance ratio between the two hind paws had a value of 1 in uninjured mice, reflecting equal pressure from both paws on the surface. We first verified that the hydrogel itself does not have any regenerative effects by comparing conditions with and without the perineural hydrogel in the absence of NMIIi2 (Supplementary Fig. S8D). After a sciatic nerve crush the mice displayed a 55% reduction of the paw luminance on the injured side on day 1 post-surgery, which persisted until day 14 (Fig. 5D–F). However, the paw luminance ratio significantly increased in the nerve NMIIi2-treated group on day 10 post-SNC injury compared to the vehicle and continued to show a substantial improvement up to 3 weeks post-injury (Fig. 5F). Recovery of paw luminescence in the vehicle group only manifested at 21 days, indicating that local NMII inhibition halved the time it took to return hindlimb motor function. Furthermore, we observed a positive correlation between the luminance ratio and percentage of pre/post-synaptic co-localization in the lumbrical muscle on day 14 post-injury, indicating that the recovery of motor behavior accurately reflects

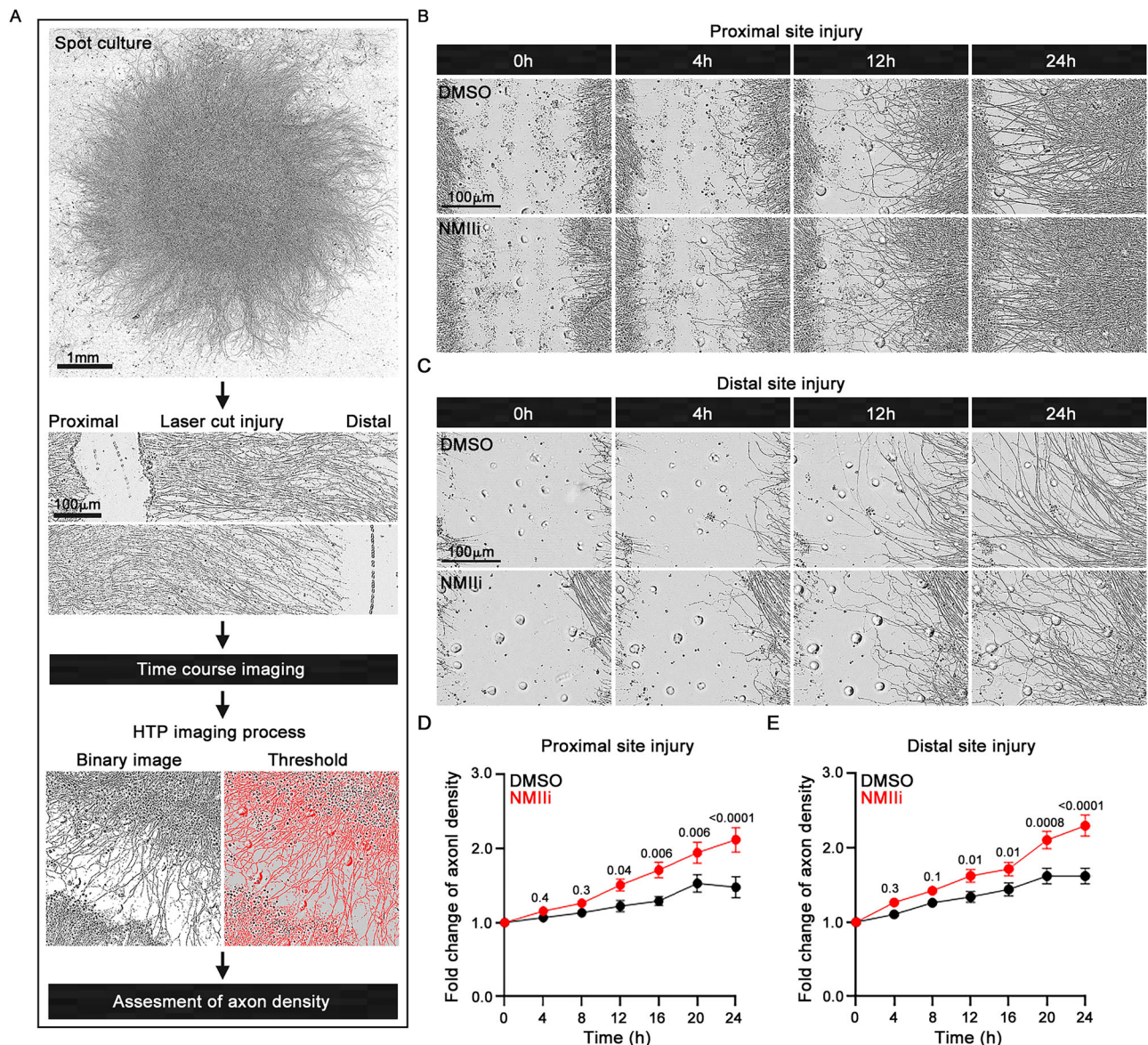


Fig. 3 | NMII inhibition promotes regeneration after axonal injury. **A** Image of a day 7 spot culture of human motor neurons with neurites projecting unidirectionally from cell bodies in the center. A laser cut injury was applied - 200 μm from the edge of the cell body cluster (proximal site injury) or - 700 μm from the cell body cluster, near the axon terminals (distal site injury). Injury size: 200–300 μm . Axon density was measured using a high-throughput SNT script that crops the injury site, adjusts the threshold, and binarizes the raw images. Images of regenerating neurons after axonal injury at proximal (**B**) or distal (**C**) sites. Scale bar: 100 μm . Quantification of axon density after a proximal (**D**) or distal injury (**E**) with DMSO or 10 μM NMIIi2. Experiments were in triplicates. Data from ≥ 2 fields per spot were quantified and normalized to DMSO. All experiments conducted in triplicate,

stats: two-way ANOVA with Tukey's *post hoc* test, SEM error bars. Spot counts and *p*-values as follows: Proximal injury (DMSO) - 0 h ($n = 12$), 4 h ($n = 12$), 8 h ($n = 11$), 12 h ($n = 12$), 16 h ($n = 12$), 20 h ($n = 12$), and 24 h ($n = 11$), and (NMIIi2) - 0 h ($n = 13$, $p = 0.98$), 4 h ($n = 13$, $p = 0.4$), 8 h ($n = 12$, $p = 0.3$), 12 h ($n = 12$, $p = 0.04$), 16 h ($n = 13$, $p = 0.006$), 20 h ($n = 13$, $p = 0.006$), and 24 h ($n = 12$, $p < 0.0001$); distal injury (DMSO) - 0 h ($n = 15$), 4 h ($n = 15$), 8 h ($n = 14$), 12 h ($n = 15$), 16 h ($n = 15$), 20 h ($n = 15$), and 24 h ($n = 13$), and (NMIIi2) - 0 h ($n = 16$, $p = 0.99$), 4 h ($n = 16$, $p = 0.3$), 8 h ($n = 15$, $p = 0.1$), 12 h ($n = 15$, $p = 0.01$), 16 h ($n = 15$, $p = 0.01$), 20 h ($n = 16$, $p = 0.0008$), and 24 h ($n = 14$, $p < 0.0001$). Data for Fig. (**D**, and **E**) are available in the Source Data file.

motor axon re-innervation of the muscle after the nerve crush injury (Fig. 5G). Local NMIIi2 treatment at the site of a nerve injury, therefore, enhances axon regeneration and thereby accelerates functional recovery.

We also examined NMJ re-innervation and motor function recovery in mice following systemic NMIIi2 administration by intraperitoneal injection (Supplementary Fig. S9A). However, there was only a minimal increase in muscle reinnervation at the dose tested (10 mg/kg twice a day) (Supplementary Fig. S9D and S9E) and no enhanced motor recovery (Supplementary Fig. S9B). Furthermore, the mice lost weight during the treatment (Supplementary Fig. S9C),

indicating that systemic exposure to NMIIi2 causes side effects without reaching a level where regeneration is enhanced, and in consequence, local administration of an NMII inhibitor to an injured nerve is both more effective, and safer.

We also examined the expression of SCG10/STMN2, a microtubule-destabilized protein that is highly expressed after injury and widely used as an injury marker in the sciatic nerve. On day 3 post-injury, SCG10/STMN2 intensity was noticeably higher in NMIIi2-treated nerves compared to the vehicle-treated mice (Fig. 6A and C). We also observed that CGRP-positive nociceptors are more prominently labeled in the NMIIi2-treated group, while the vehicle-treated group

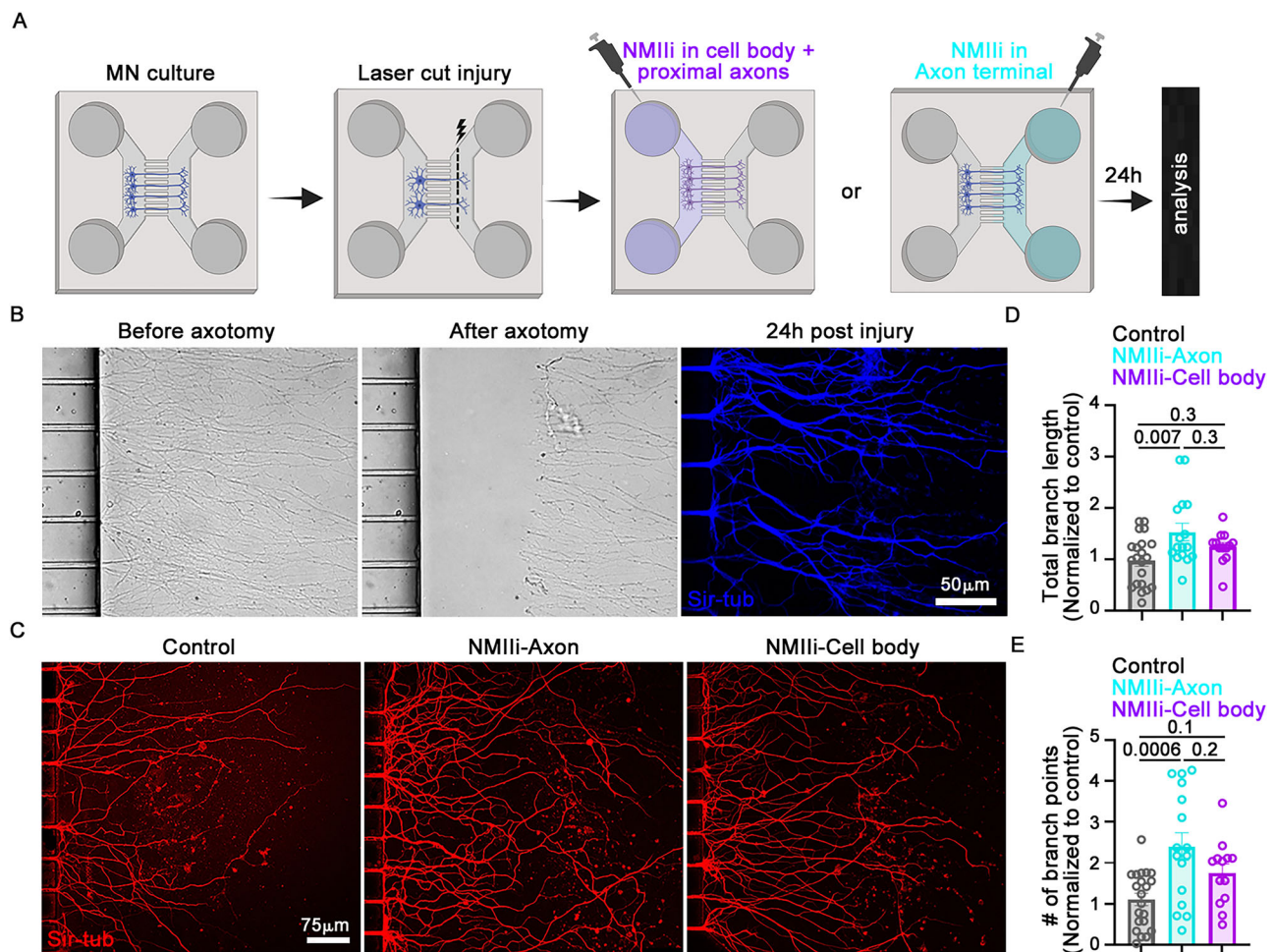


Fig. 4 | NMII inhibition of injured axons increases neurite length and branching. **A** Schematic of local NMII2 incubation of motor neuron cell bodies/proximal axons or distal axons in a microfluidic device and of the site of the axonal injury, by BioRender. Zeng, X. (2025) <https://BioRender.com/i63w966>. **B** Images of neuronal projections passing across microfluidic device microgroove before and after axotomy. Regenerating axons labeled by Sir-tub 24h-post injury **(C)** Representative images of regenerated axons incubated with DMSO, 10 μ M NMII2 in either the axonal or cell body site for 24 h after a laser cut axonal injury. Images by confocal

microscope, microtubules labeled with Sir-tub. Scale bar: 75 μ m. **D, E** Quantification of total branch length and branch points. Data normalized to DMSO. Results were compiled from 21 microfluidic devices for the control group, 16 for NMII2 treatment of distal axons, and 13 for NMII2 treatment of cell bodies. Experiment conducted in four replicates. Statistical analysis: nonparametric Kruskal–Wallis test with Dunn’s multiple comparison test for **(D)** and two-sided Welch’s test with Dunnett’s multiple comparison test for **(E)**, SEM error bars. *P*-values are indicated on the graph. Data for Fig. **(D, E)** are available in the Source Data file.

showed more limited regeneration (Fig. 6A and C). We also assessed the regeneration of NF-labeled axons and found that these also regenerate faster after NMII2 treatment on day 3 and day 7 post-injury (Fig. 6B and Supplementary Fig. S7A), revealing enhanced regeneration across multiple sensory neuronal subtypes.

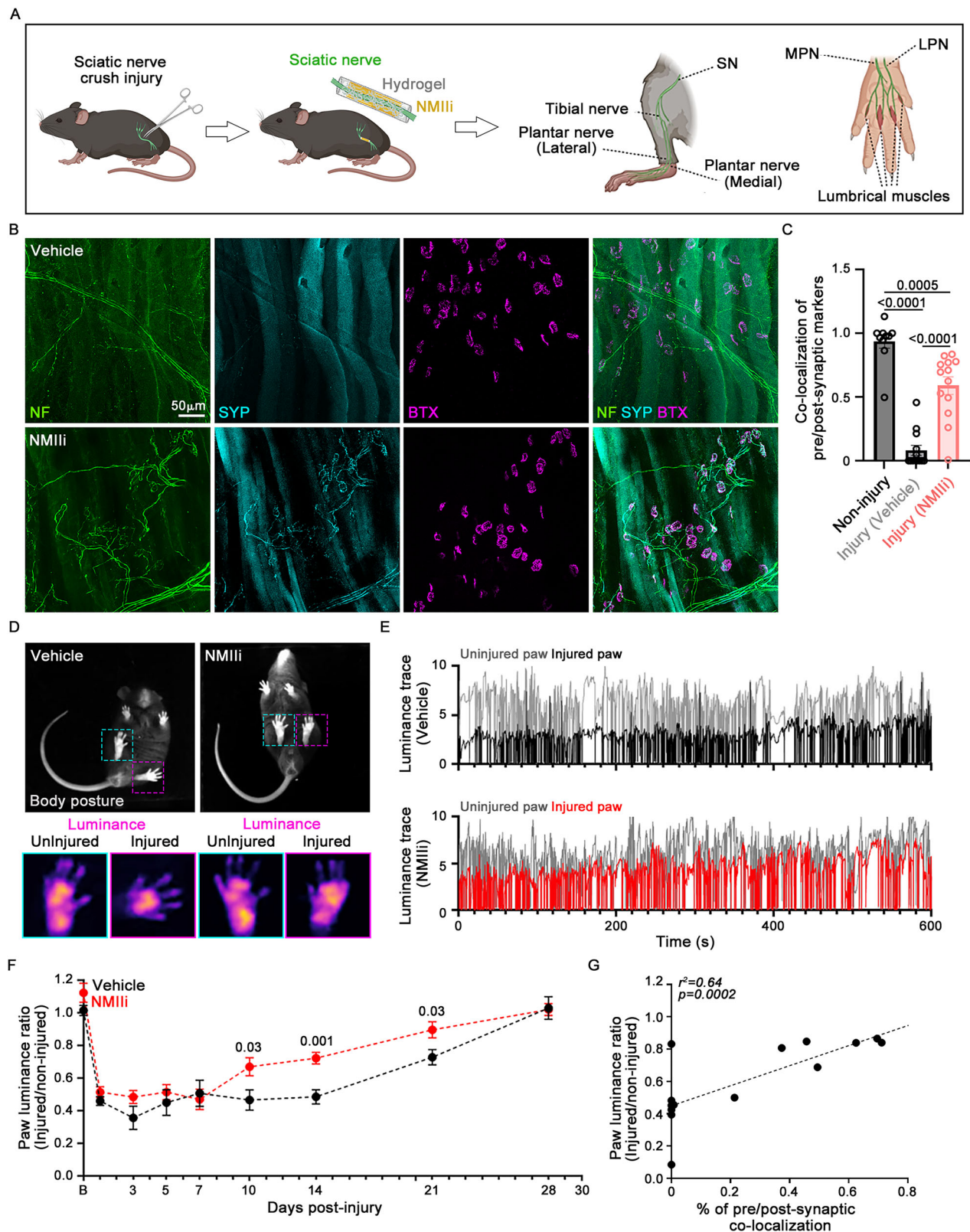
We also assessed sensory recovery, using a skin pinprick assay, as described previously³. Briefly, we measured mouse nociceptive reactions to pinprick stimulation of the lateral area of the paw, in which the sciatic nerve innervates and is denervated by a crush injury. The NMII2-treated group exhibited a significantly improved sensory response to pinprick by day 7 post-injury, compared to the vehicle-treated mice (Fig. 6D). These data reveal that NMII2 promotes functional regeneration of sensory neurons. The data show, moreover, that sensory and motor components recover at different times: sensory recovery is evident by day 7, whereas motor recovery only becomes prominent by day 14. This temporal difference underscores that the machine-learning approach is particularly effective for evaluating motor function recovery, as revealed by the positive correlation between paw luminance ratio and lumbrical muscle reinnervation (Fig. 5G) but not with nocifensive responses to noxious stimuli (Fig. 6E). NMII2 treatment promotes, therefore, functional

recovery in vivo across multiple neuronal populations in the peripheral system.

Lastly, we conducted additional immunohistochemistry experiments to evaluate if there are changes in Schwann cells (S100+), immune cells (CCR2+), and activated fibroblasts (FAP+) following local NMII2 administration to the sciatic nerve injury site in mice. We assessed changes on day 3 post-injury, a time point where these non-neuronal cells actively react to a nerve crush injury³⁶. However, we found that none of these cell types showed any major changes in the NMII2-treated group compared to the vehicle-treated group (Supplementary Fig. S10A–S10C). This suggests that NMII2 specifically targets axons in vivo, which is compatible with the in vitro data.

Discussion

Peripheral nerve injuries often result in prolonged sensory and motor disabilities, which pose significant clinical challenges to patients. Despite major advances in our understanding of neuronal regeneration in the PNS, achieving a full functional recovery following such injuries remains elusive, which may be largely the consequence of the slow rate of axonal regrowth. Our study was designed to address this problem by exploring the therapeutic



potential of a target identified from a human motor neuron phenotypic screen designed to detect axon regeneration promoters. This phenotypic platform is also applicable to other neuronal types. Our primary screening platform identified drugs that promoted the regeneration of motor neurons both in a CNS-like (CSPG) and PNS-like (laminin) environment. For secondary screening, we assessed both regeneration responses following

axon injury using a laser to transect axons in a spot culture and also observed the site of action with a microfluidic device. The in vitro screen revealed NMII to be a major target for increasing axon regeneration and that its inhibition at the site of an axon injury promotes axon growth, which was fully replicated in vivo, which indicates that the platform can successfully identify potential novel therapeutic interventions.

Fig. 5 | NMIII2 at sciatic nerve injury site accelerates motor function recovery in mice. **A** NMIII2 was delivered locally to sciatic nerve crush injury site packaged with a hydrogel scaffold in a silicone tube and motor behavior was assessed at different time points and lumbrical muscles dissected from mouse paw of day 14 post injury, schematic by BioRender. Zeng, X. (2025) <https://BioRender.com/b18q366>. **B** Representative images of lumbrical muscles day 14 post-injury from mice treated by local application of vehicle or NMIII2 labeled with anti-neurofilament (NF), anti-synaptophysin (SYP) or α -bungarotoxin (BTX). **C** Co-localization of pre/post-synaptic markers per muscle in mice with intact sciatic nerve (non-injury) and 14 days post-nerve injury. Number of presynaptic markers that overlap with the postsynaptic marker, α -bungarotoxin normalized to post-synapse (α -bungarotoxin) number.

Stats: nonparametric Kruskal–Wallis test with Dunn’s multiple comparison test, SEM error bars. *P*-values indicated on the graph. Data collected from 13 male mice/group. **D** Representative mouse paw luminance signals on day 14 post-injury. Paw on non-injured side (cyan), injured side (magenta). **E** Density histogram of right and left paw surface contact on day 14 post-injury in response to local administration of vehicle or NMIII2. **F** Quantification of luminance ratio of left/right paws post sciatic nerve crush. Stats: two-way ANOVA with Tukey’s *post hoc* test, SEM error bars, 8 male mice per condition. **G** Two-sided Pearson correlation between the paw luminance ratio and percentage of pre/post-synaptic colocalization from the same mouse shown in panel (C). Data collected from 16 male mice per group. Data for Fig. (C, F, and G) are available in the Source Data file.

Both axonal elongation and arborization post-nerve injury are crucial for effective functional recovery, as the first ensures the axon reaches its target, and the second increases the chances of the establishment of an effective functional reconnection. Previous studies have shown that NMII inhibitors promote branching in non-neuronal cells^{37,38}. However, whether they increase axonal elongation in motor neurons after a traumatic nerve injury has not been investigated before. Our results demonstrate that NMII inhibitors promote elongation of injured axons. One possible mechanism of this involves the Rho/ROCK pathway. Inhibition of Rho/ROCK leads to increased F-actin destabilization through profilin dephosphorylation, resulting in enhanced branch arborization^{9,39,40}. Rho/ROCK also activates myosin II contractility^{38,41,42}. Based on these studies, we speculate that myosin II in injured axons, when activated by Rho/ROCK, reduces axonal growth. Our compound screen, in addition to identifying the NMII inhibitor blebbistatin, also identified four ROCK1/2 inhibitors (Fig. 1F) supporting the engagement of this pathway in axonal regeneration.

Another possibility is that NMII inhibition promotes neurite outgrowth via Rho/ROCK-independent mechanisms. While local myosin II assembly reduces cell-surface curvature via actomyosin tension, the cell surface could regulate myosin II stabilization and F-actin binding in a Rho/ROCK independent manner, which are then stabilized by adhesion molecules on the extracellular matrix (ECM), leading to the formation of more protrusions^{20,37,38,43,44}. Understanding this process will be critical for explaining how NMII inhibitors can simultaneously both enhance branch protrusion and elongation. Our study has demonstrated that NMII inhibitors promote branch protrusion and growth cone dynamics, as evident by the thin growth cones lacking lamellipodia after periphery nerve injury. Also, the rapid manifestation of this growth-promoting phenotype following treatment (Fig. 4D and E), indicates that the regenerative effects are likely driven by activity-dependent or post-translational mechanisms rather than transcriptional changes. Our study identifies a potential positive feedback loop mechanism involving myosin II stabilization and myosin II activity in injured axons following NMIII2 treatment. However, further studies are required to expand our understanding of how NMII inhibitors can simultaneously enhance myosin II stabilization while modulating myosin II activity.

Nerve transection injury models typically show minimal functional recovery⁷. In contrast, nerve crush injury enables nerve regeneration and recovery of motor and sensory function and is, therefore, frequently used in regeneration studies. Inhibition of NMII with NMIII2 in mice after a sciatic nerve crush injury was evaluated through two approaches: local and systemic administration. Silicone-based implants, because of their biocompatibility⁴⁵, were chosen to provide localized, controlled drug delivery directly to the injured axons. Injured sciatic nerves regenerated more rapidly with increased reinnervation of target muscles following NMIII2 administration restricted to the nerve injury site (Fig. 5C), leading to accelerated functional recovery (Fig. 5F). However, systemic NMIII2 application had an inconsistent action on injured axons (Supplementary Fig. S9E) and no motor function recovery (Supplementary Fig. S9B). Furthermore, systemic administration for longer than three days led to marked

weight loss (Supplementary Fig. S9C). This suggests that NMIII2 may target myosin IIs in non-neuronal cell types and that this inhibition results in cytotoxicity. However, the toxic effects and lack of efficacy after systemic administration were completely overcome by local administration at the site of nerve injury, and this may well be a useful strategy for patients. Our study also demonstrates that hydrogel-based local delivery is an effective method for investigating nerve regeneration. Our analyses indicate that the hydrogel released NMIII2 for approximately 3–7 days post-application. Once the regenerating axons grew beyond the hydrogel-embedded lesion site, the localized effects of NMIII2 diminished, highlighting the importance of an early, targeted local intervention. These findings reinforce the therapeutic potential of localized NMII inhibition, in spite of the limitations of systemic delivery.

Local NMIII2 treatment both accelerated axon regrowth and increased the number of functional NMJs, which may be due to a promotion of axon branching. Myosin II inhibition may act by modifying F-actin polymerization and internal hydrostatic pressure, which affects the stabilization of adhesion molecules such as integrins to the extracellular matrix^{38,44,46}. Once branches are formed, they may either remain or retract⁴³, and our data indicates retention of the neuromuscular junction. For successful regeneration after a nerve injury, it is crucial to overcome the damaged environment and activate axonal growth mechanisms to ensure functional reconnection with appropriate targets, all of which we find was facilitated by local administration of an NMII inhibitor directly to the site of injury. We conclude, therefore, that local NMII inhibition is a promising approach to enhance functional recovery of nerves injured by trauma, surgery, or compression, and possibly also for conditions like diabetic neuropathy or chemotherapy-induced neuropathy, which need to be examined.

Mechanoreceptor and proprioceptor sensory neurons play a crucial role in sensorimotor feedback and motor function recovery after nerve injury^{47–49}. Our paw luminance data likely reflect motor behavior primarily driven by motor axon regeneration but may also capture contributions from the regeneration of those proprioceptor and mechanoreceptor axons. Supplementary Fig. S7A shows that NF-positive but ChAT-negative axons are present in regenerating nerves after local NMIII2 treatment, suggesting that proprioceptor and mechanoreceptor sensory neurons also regrow faster. These findings imply that the motor function recovery after NMIII2 could be the result of both accelerated motor and sensory neuron regeneration. Identification of the specific actions of NMIII2 on those different sensory subtypes which contribute to motor function recovery would provide valuable insights into the utility of this approach for promoting a full recovery of motor function.

The development of a human neuron phenotypic platform that captures those compounds which promote axon regeneration and is predictive of positive activity in vivo can aid both a greater understanding of the mechanisms that drive axon regeneration and target tissue reengagement and contribute to the development of novel therapeutic strategies for overcoming neuronal damage in the adult nervous system. We speculate that NMIII2 may promote the growth of central neurons on CSPG substrates independently of integrin

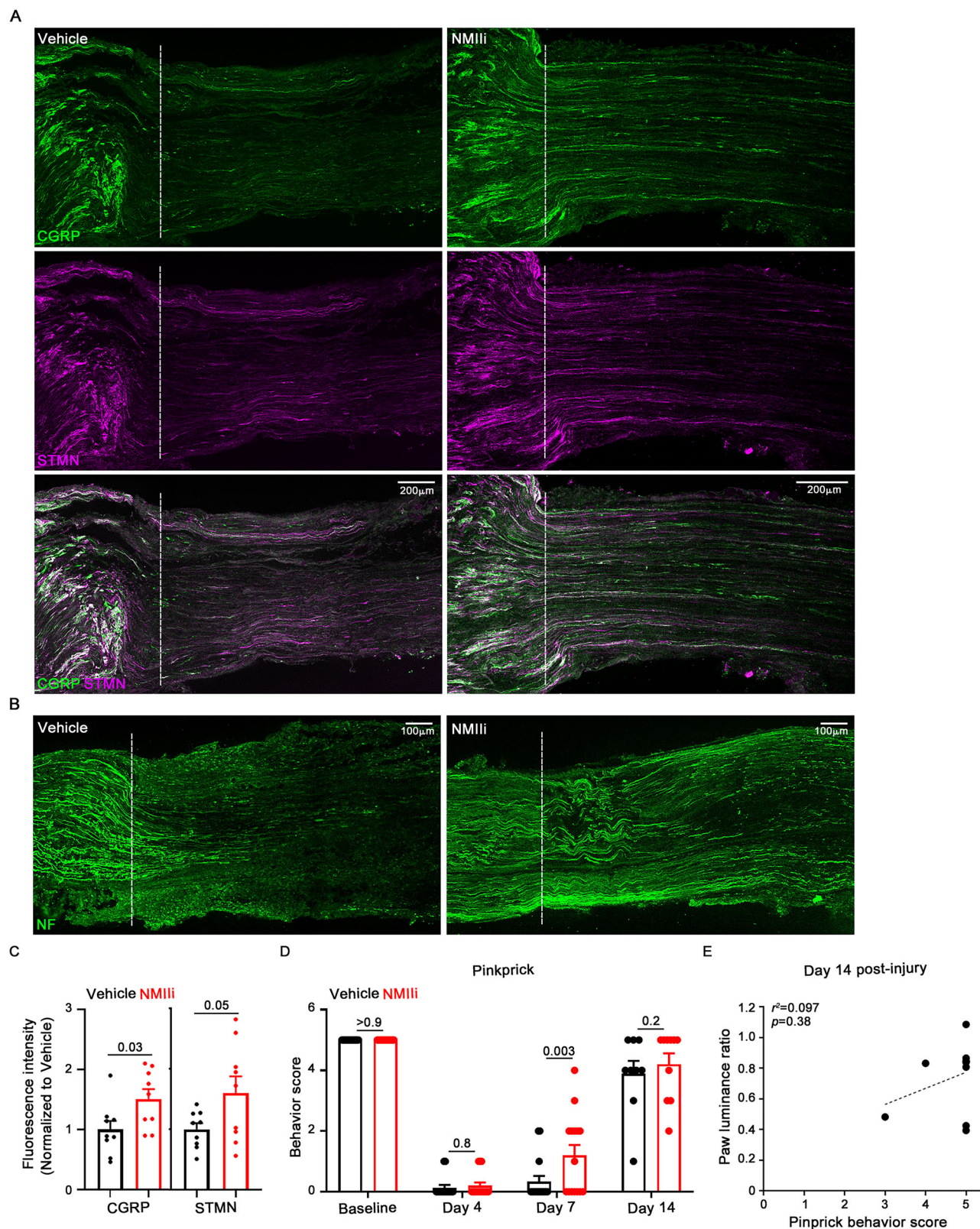


Fig. 6 | NMII2 applied at the sciatic nerve injury site promotes sensory axon regeneration and functional recovery. **A** and **B** Representative images of mouse sciatic nerves day 3 post-injury treated with local application of either vehicle or NMII2 and labeled with anti-CGRP (green), anti-stathmin (magenta) (**A**), and anti-neurofilament (green) (**B**), white dashed lines indicate the boundary of the crush injury site. **C** Quantification of CGRP and stathmin intensity from regenerated axons. Data collected from 3 mice per group and normalized to vehicle condition.

Statistics: unpaired two-tailed Student's *t*-test, SEM error bars. **D** Score of pinprick tests following local application of vehicle or NMII2 at baseline and day 4, 7, and 14 post-injury. Statistics: two-way ANOVA with Tukey's *post hoc* test, SEM error bars, 15 mice per condition. **E** Two-sided Pearson correlation analysis of the paw luminance ratio (Injured/Non-injured) and pinprick behavior scores on day 14 post-injury. Data collected from 10 male mice per group. Data for Fig. C-E are available in the Source Data file.

regulation. However, in the PNS, integrins likely play a more prominent role in regeneration, as described by the molecular clutch model⁵⁰, which highlights two key contributions of integrins to growth cone dynamics: regulation of actin retrograde flow and generation of mechanical forces through integrin-ECM interactions at the growth cone. In contrast, CNS neurons are surrounded by a perineuronal net (PNN) composed of CSPGs^{14,51}. This may explain why integrins have a more substantial impact on promoting regeneration in the PNS compared to the CNS. NMII inhibition acts both on neurons with axons in the PNS as well as those restricted to the CNS, indicates that local application of NMII inhibitors to injured axons within the CNS may enhance regeneration after spinal cord or brain injury, which now needs to be tested.

Methods

Ethical statement

All animal experiments were performed in accordance with protocols approved by the Institutional Animal Care and Use Committee (IACUC) at Boston Children's Hospital (Protocol number: 00001507). Experimental procedures involving human stem cell lines were conducted at Boston Children's Hospital under IRB approval (IRB-P00006313).

Compound Library

The compound library used for the primary screen was supplied by the ICCB-Longwood Screening Facility (Harvard Medical School) and included most known bioactives from Biomol ICCBL Known Bioactives 2012 Library, Mechanism of Action Library, Prestwick 3 collection, and Selleck bioactive library. The primary screen used a drug concentration of 15 μ M, except for the Biomol library, where concentrations varied up to 0.1 mM based on potency and availability.

Synthesis of compound and bioassays

The blebbistatin analog NMII2 was synthesized as previously reported²⁹. Photostability, EC50 values (μ M) for the inhibition of non-myosin II, and Ki values (μ M) for the inhibition of cardiac myosin II were measured as described in ref. 29. NMII2 was confirmed to cross the blood-brain barrier, as indicated by a Kp (brain/plasma) value of 2.32, measured from three mouse brains.

shRNA constructs

Scrambled shRNA (#SHC216), and *MYH9 shRNA* (#276055) were obtained from Sigma Aldrich. *pLV-scramble shRNA* and *pLV-MYH9 shRNA* expressing lentivirus were produced at Boston Children's Hospital Viral Core. The virus was administered to neurons at a multiplicity of infection of 10.

Cell culture

Motor neuron differentiation. Human iPSCs (hiPSCs) were obtained from following: SAH-0047 from a 46-year-old female donor (Mustafa Sahin lab at Boston Children's Hospital), LiPSC-GRL1 from a male newborn donor (Lonza) and 11a from a 36-year-old male donor (Kevin Eggan lab⁵²), were maintained in StemFlex medium (#A3349401, Thermo Fisher) on geltrex (#A1413302, Thermo Fisher) coated plates. hiPSCs were dissociated using ReLeSR (#05872, Stem Cell Technologies) for passaging. The primary screen was conducted using SAH-0047, while the secondary screen utilized the Lonza and 11a lines. hiPSCs were differentiated to motor neurons followed by a two-week differentiation protocol³⁰. On Day 14 post-differentiation, the cells were dissociated to single cells with accutase (#AT104, Innovative Cell Tech) and sorted by magnetic-activated cell sorting approach using human CD56 neural cell adhesion molecule 1 antibody (#555516, BD Biosciences) and anti-R-phycoerythrin magnetic particles (#557899, BD Biosciences). For primary screen, 8000 sorted motor neurons per well were plated on 100 μ g/mL poly-D-Lysine (#P6407, Sigma-Aldrich) or 0.2 ng/mL CSPG (#CC117, Millipore)-coated 96-well plate (#655090,

Greiner Bio-One) and maintained in motor neuron media composed of neurobasal-A medium (#10888-022, Life Technologies) supplemented with 1x B27 (#17-504-044, Gibco), 1x N2 (#17-502-048, Gibco), 1x GlutaMAX (#35050-061, Life Technologies) and 100 μ M non-essential amino-acids (#11140-050, Life technologies). Additionally, 35 μ g/mL ascorbic acid (#a4403, Sigma-Aldrich), 10 ng/mL of recombinant human BDNF (#PHC7074, Thermo Fisher), GDNF (#450-10, Pepro-Tech) and CNTF (#PHC7015, Thermo Fisher) were added prior to feeding. For growth permissive condition, 8000 cells per well were plated on 100 μ g/mL poly-D-Lysine (#P6407, Sigma-Aldrich) or 10 μ g/mL laminin (#23017015, Thermo Fisher)-coated 96-well plate.

Spot culture. 5 μ L motor neuron medium containing around 250,000 motor neurons were plated at the center of 24-well plates coated with 25 μ g/mL poly-L-Ornithine (#P4957, Sigma-Aldrich) and 10 μ g/mL laminin. After 1 h, the rest of the media is replenished and fed every 3 days by half-medium changes. To examine injury response, compounds were added to spot cultures after the laser axotomy with a 300 mW Stiletto infrared laser (Hamilton Thorne).

Neurons in microfluidic device. 500,000 motor neurons were seeded per microfluidic device (#SND450, Xona microfluidics) on a 55 mm glass bottom dish (#D60-30-1.5-N, Cellvis) after coated with 25 μ g/mL poly-L-Ornithine in 1.34x Borate buffer (#28341, Thermo Fisher) and 10 μ g/mL laminin. The cells are maintained for 5 days in a motor neuron medium. 10 μ M NMII2 was treated locally to distal axons or cell body using gradient flow in microfluidic devices followed by laser cut injury at distal axons. At 24 h post-injury, SiR-tubulin dye (cy-sc002, Cytoskeleton) was added to label the regenerated neurons.

For dissociated DRG cultures, L3-L6 DRGs were extracted from P30 mice on ice, digested, and dissociated in HEPES buffer containing Dispase (Roche) with collagenase A (Roche). The dissociated cells were seeded on one side of microfluidic devices after coated with 100 μ g/mL poly-D-Lysine and 25 μ g/mL laminin. After 48 h, a laser cut injury was applied to the distal axons, and NMII2 was applied only to the distal axons. At 48 h post-injury, regrowing neurons were labeled with SiR-tubulin dye.

Cortical neuron differentiation. Human ESCs (WA09, WiCell) were obtained from the UCLA Broad Stem Cell Research Center and maintained in mTeSR Plus medium (StemCell Technologies) on Cultrex (Biotechnology) coated plates. Inducible human NGN2 was stably integrated into the AAVS1 safe harbor locus using eSpCas9(1.1)_No_FLAG_AAVS1_T2 as described⁵³ (a gift from Yannick Doyon) and a donor plasmid containing doxycycline-inducible human NGN2 and a zeocin selection marker⁵⁴. Induced neurons were generated as described⁵⁵. Briefly, stem cells were induced with 2 μ g/mL doxycycline (Sigma Aldrich) in mTeSR Plus medium for two days. Starting on the second day of induction, 2.5 μ g/mL zeocin (Thermo Scientific) was also added to the medium. From the third to seventh day, cells were cultured in Neuronal Maturation Medium (NMM), which contained 1/2 DMEM/F-12 and 1/2 Neurobasal media (Gibco) supplemented with N-2 (Gibco), B27 (Gibco), 1 μ g/mL laminin (Corning), doxycycline, and zeocin. Human cortical organoids were a gift from the Aparna Bhaduri lab at UCLA. Cortical organoids were generated with the human ESCs UCLA6 from the UCLA Broad Stem Cell Research Center, followed by an adaptation of the Kadoshima protocol^{56,57}. Induced neurons and cortical organoids were dissociated with TrypLE (Gibco) and the Papain Dissociate System (Worthington), respectively. Cells were plated onto black-walled Greiner CELLSTAR μ Clear 96-well plates coated with 5 μ g/mL laminin or 0.2 ng/mL CSPG.

Retinal ganglion cells culture. Retinal ganglion cells (RGCs) were purified from the eyes of 6-8-week-old female mice as described in reference⁵⁸. Subsequently, 200,000 dissociated RGCs were seeded

into the wells of 24-well plates (#82426, ibidi) coated with 20 µg/mL poly-L-ornithine and 10 µg/mL laminin. On the seeding day, NMII inhibitors were added, and the cells were incubated for three days.

Image acquisition and analysis from human neurons

Live cell imaging was performed by 10x objective and quantified for total neurite length per field using an InCuCyte S3 Live-Cell Analysis System (Sartorius). Fixed motor neurons with 4% paraformaldehyde (Electron Microscopy Sciences) were immunolabeled with a mouse antibody against β III-tubulin (#T8660, Sigma) and Hoechst 33342 (#1399, Thermo Fisher). Then, the cells were imaged with a 10x objective and 2 × 2 binning using an ArrayScan XTI imaging platform (Thermo Fisher), and the total neurite length per neuron and neuron number quantified in a customized script in the XTI platform. Images from microfluidic devices were captured using a Leica SP8 confocal microscope. To quantify total branch length and branch points, a customized code that allows for measurement in a high-throughput manner for SNT and Sholl analysis were used in Fiji (ImageJ). Fixed-induced neurons and cortical organoids were immunolabeled for β III-tubulin (eBioscience) and Hoechst 33342 (Thermo Fisher) and imaged at UCLA's Molecular Screening Shared Resource on an Image Xpress MicroXL (Molecular Devices) and neurite length was measured using IN Carta (Molecular Devices) automated analysis. Cell viability following treatment with the top compounds identified in the screen was measured using a viability/cytotoxicity assay (#L3224, Invitrogen)³³. Briefly, 2 µM Calcein-AM and 4 µM EthD-1 were treated for 20 min in an incubator prior to imaging. Live cell imaging was done with a 10x objective and intensity of Calcein, and EthD-1 quantified using an InCuCyte.

Western blots

Human-derived motor neurons were homogenized in cold NP40 lysis buffer (#J60766-AP, Thermo Fisher) containing a protease inhibitor cocktail (#1183617000, Roche). Protein concentration was measured using BCA protein assay kit (Thermo Fisher). were separated using 4–12% gradient SDS-PAGE gel electrophoresis and then transferred to nitrocellulose membranes (#LC2001, Invitrogen). The membranes were blocked with 5% skim milk in Tris buffer containing 0.1% Tween 20 for 1 h at room temperature and subsequently probed with primary antibodies. The primary antibodies were used anti-myosin IIA (1:1000; #3403, Cell Signaling) and anti-GAPDH (1:500; #MA5-15738, Thermo Fisher). The membranes were then incubated for 2 h at room temperature with secondary antibodies, anti-rabbit and anti-mouse (Licor Biosciences), at 1:5000. The images captured and the band intensity from images were analyzed using Image Studio software (Licor Biosciences).

Mouse surgical procedures and behavior test

8-week-old male C57BL/6J mice were obtained from Jackson Laboratory (#000664). Sciatic nerve crush surgery and subsequent local application were performed aseptically under 2% isoflurane anesthesia^{7,59}. The left sciatic nerve trunk, including the sural, common peroneal, and tibial nerves, was crushed for 20 s using a hemostat. For the local application of NMII2, a 2.5 mm long silicone tube cuff (Dow Corning) with an inner diameter of 0.635 mm was positioned around the injury site immediately after the crush injury. The cuff was further secured to the nerve using 10-0 polypropylene sutures (Ethicon). Either 100 µM NMII2 dissolved in the vehicle with Lifeink 200 Hydrogel (#5278, Advanced BioMatrix) or the vehicle with hydrogel alone was injected into the cuff. The surgical incisions were closed with 6-0 sutures (Ethicon). For systemic application, 10 mg/kg of NMII2 was administered via intraperitoneal injection twice daily for three consecutive days. To assess motor functional recovery, lumbrical muscles were dissected⁶⁰ immediately following the paw luminance assessment to evaluate NMJ recovery and its correlation with functional recovery. The flexor tendons and the flexor digitorum longus tendon

were exposed, and then the lumbrical muscles between the second and third, or third and fourth toes extracted under a dissection microscope. The extracted muscles were processed for NMJ staining as described above. The behavioral tests were conducted between 1:00 PM and 3:00 PM for all animals at all time points. The duration of the walking track measurement was 10 min. Paw luminance was extracted and analyzed as described³⁵. A correlation analysis between the number of NMJ innervations and the luminance ratio for each animal was performed to assess functional recovery. Pinprick sensory tests were performed as described⁷. Briefly, mice were placed in wire mesh chambers and habituated over three sessions (each 60 minutes) during the week prior to the injury, followed by a baseline assessment. Postoperative tests were conducted on the days specified in Fig. 5D. An insect pin was applied to the lateral plantar surface of the paw five times with intervals of 3–5 min between applications. A response was recorded as positive (scored as 1) if the animal briskly withdrew its paw; otherwise, the score was recorded as 0. All tests were performed by an investigator blinded to the treatment.

Immunohistochemistry, image acquisition and analysis from mouse tissue

Dissociated RGCs were fixed with cold 4% paraformaldehyde, permeabilized with 0.3% Triton X-100 in PBS for 10 min, and blocked with 1% BSA in PBS with 0.1% Triton X-100 for 1 h at room temperature. Primary antibody incubation was done overnight at 4 °C with RBPMs antibody (#NBP2-80389, NovusBio), and secondary antibody incubation were done with Alexa Fluor 594 guinea pig antibody (#706-585-148, Jackson ImmunoResearch) for 2 h at room temperature. Images were captured using a Leica SP8 confocal microscope. For quantification, a customized SNT script was used in Fiji (ImageJ). Lumbrical muscles of the hind paw innervated by plantar nerves originating from the sciatic nerve, were dissected from mice after the functional tests⁶¹ and immunolabeled as detailed before⁶². Briefly, muscles are fixed with cold 4% paraformaldehyde for 10 min, permeabilized with 2% Triton X-100 in PBS for 30 min, and blocked with 5% normal donkey serum and 5% normal goat serum in PBS with 1% Triton X-100 in PBS for 1 h at room temperature. Primary antibody incubation was done overnight at 4 °C using anti-Synaptophysin (#ab32127, Abcam) and anti-Neurofilament (#AB5539, Millipore) to label neurons and the pre-synaptic terminal. Samples were further incubated with the following antibodies: Alexa Fluor 488 rabbit antibody (#A11008, Invitrogen), Alexa Fluor 488 chicken antibody (#703-545-155, Jackson ImmunoResearch), and Alexa Fluor 647 conjugated α -bungarotoxin (#B35450, Thermo Fisher) overnight at 4 °C. Dissected sciatic nerves were sequentially fixed with 4% paraformaldehyde overnight at 4 °C, cryoprotected with 30% sucrose in PBS overnight at 4 °C, and sectioned at 50 µm. Sliced nerves were permeabilized with 0.3% triton X-100 in PBS for 10 min, blocking with 2% BSA in PBS with 0.1% Triton X-100 in PBS for 1 h at room temperature. Primary antibody incubation was carried out overnight at 4 °C using the following antibodies: anti-ChAT (#AB144P, Millipore), CGRP (#ab36001, Abcam), STMN (#NBPI-49461, Novus Biological), S-100 (#ab34686, Abcam), FAP (#FAB9727G, R&D system) and CCR2 (#NBPI-48338, Novus Biological). Secondary antibody incubation was done for 2 h at room temperature with following: Alexa Fluor 568 goat (#A11057, Invitrogen), Alexa Fluor 488 rabbit (#A11008, Invitrogen), Alexa Fluor Cy5 rabbit (#711-175-152, Jackson ImmunoResearch), and Alexa Fluor 488 goat (#A11055, Invitrogen). Images were captured with a Leica SP8 confocal microscope, and α -bungarotoxin-labeled postsynaptic clusters were manually scored from maximum projection images. Pre- and postsynaptic colocalization was assessed using z-stacked images.

Statistical analysis

Values are expressed as means ± SEM or means ± SD. Statistical analyses were conducted as follows: for comparisons between two groups,

unpaired two-tailed Student's *t*-tests were used. For comparisons involving more than two groups, the normality of mean values was assessed using the D'Agostino and Pearson omnibus normality test, and variance evaluated with Bartlett's test; otherwise, the Kruskal–Wallis test with Dunn's multiple comparison test or Welch's test with Dunnett's multiple comparison test were used. For time-course measurements, a two-way ANOVA followed by Tukey's *post hoc* test for multiple comparisons was employed. The *p*-value for the Pearson correlation coefficient was calculated using the *t*-statistic. Graphs were plotted using GraphPad Prism.

Reporting summary

Further information on research design is available in the Nature Portfolio Reporting Summary linked to this article.

Data availability

The data from this study are available in the main paper and Supplementary Information, with all source data included. We did not reuse existing datasets. Due to the substantial storage requirements for our raw images and video data, there are technical challenges in depositing these files in a public repository. However, to ensure transparency and data accessibility, we are happy to provide raw video data and source images upon reasonable request. Source data are provided in this paper.

Code availability

The ImageJ codes used to quantify regenerating axons in spot cultures are publicly available at GitHub [<https://github.com/selwynjayakar/Multi-image-neurite-analysis>]. The relevant data generated in this study are provided in the Supplementary Information/Source Data file.

References

- Jain, N. B. et al. Traumatic spinal cord injury in the United States, 1993–2012. *JAMA* **313**, 2236–2243 (2015).
- Gordon, T., Tyreman, N. & Raji, M. A. The basis for diminished functional recovery after delayed peripheral nerve repair. *J. Neurosci.* **31**, 5325–5334 (2011).
- Grinsell, D. & Keating, C. P. Peripheral nerve reconstruction after injury: a review of clinical and experimental therapies. *Biomed. Res Int.* **2014**, 698256 (2014).
- Lundborg, G. A 25-year perspective of peripheral nerve surgery: evolving neuroscientific concepts and clinical significance. *J. Hand Surg. Am.* **25**, 391–414 (2000).
- Novak, C. B., Anastakis, D. J., Beaton, D. E., Mackinnon, S. E. & Katz, J. Biomedical and psychosocial factors associated with disability after peripheral nerve injury. *J. Bone Jt. Surg. Am.* **93**, 929–936 (2011).
- Songcharoen, P., Wongtrakul, S., Mahaisavariya, B. & Spinner, R. J. Hemi-contralateral C7 transfer to median nerve in the treatment of root avulsion brachial plexus injury. *J. Hand Surg. Am.* **26**, 1058–1064 (2001).
- Ma, C. H. et al. Accelerating axonal growth promotes motor recovery after peripheral nerve injury in mice. *J. Clin. Invest.* **121**, 4332–4347 (2011).
- Dent, E. W. & Gertler, F. B. Cytoskeletal dynamics and transport in growth cone motility and axon guidance. *Neuron* **40**, 209–227 (2003).
- Lowery, L. A. & Van Vactor, D. The trip of the tip: understanding the growth cone machinery. *Nat. Rev. Mol. Cell Biol.* **10**, 332–343 (2009).
- Coles, C. H. & Bradke, F. Coordinating neuronal actin-microtubule dynamics. *Curr. Biol.* **25**, R677–R691 (2015).
- Dupraz, S. et al. RhoA Controls axon extension independent of specification in the developing brain. *Curr. Biol.* **29**, 3874–3886 (2019).
- Sayyad, W. A., Amin, L., Fabris, P., Ercolini, E. & Torre, V. The role of myosin-II in force generation of DRG filopodia and lamellipodia. *Sci. Rep.* **5**, 7842 (2015).
- Solecki, D. J. et al. Myosin II motors and F-actin dynamics drive the coordinated movement of the centrosome and soma during CNS glial-guided neuronal migration. *Neuron* **63**, 63–80 (2009).
- Vicente-Manzanares, M., Ma, X., Adelstein, R. S. & Horwitz, A. R. Non-muscle myosin II takes centre stage in cell adhesion and migration. *Nat. Rev. Mol. Cell Biol.* **10**, 778–790 (2009).
- Allingham, J. S., Smith, R. & Rayment, I. The structural basis of blebbistatin inhibition and specificity for myosin II. *Nat. Struct. Mol. Biol.* **12**, 378–379 (2005).
- Melli, L. et al. Bipolar filaments of human nonmuscle myosin 2-A and 2-B have distinct motile and mechanical properties. *Elife* **7**, e32871 (2018).
- Porro, C., Pennella, A., Panaro, M. A. & Trotta, T. Functional role of non-muscle myosin II in microglia: An updated review. *Int. J. Mol. Sci.* **22**, 6687 (2021).
- Bond, L. M., Tumbarello, D. A., Kendrick-Jones, J. & Buss, F. Small-molecule inhibitors of myosin proteins. *Future Med. Chem.* **5**, 41–52 (2013).
- Wang, F. et al. Kinetic mechanism of non-muscle myosin IIB: functional adaptations for tension generation and maintenance. *J. Biol. Chem.* **278**, 27439–27448 (2003).
- Kovacs, M., Wang, F., Hu, A., Zhang, Y. & Sellers, J. R. Functional divergence of human cytoplasmic myosin II: kinetic characterization of the non-muscle IIA isoform. *J. Biol. Chem.* **278**, 38132–38140 (2003).
- Radnai, L., Stremel, R. F., Sellers, J. R., Rumbaugh, G. & Miller, C. A. A Semi-high-throughput adaptation of the NADH-Coupled ATPase assay for screening small molecule inhibitors. *J. Vis. Exp.* **150**, <https://doi.org/10.3791/60017> (2019).
- Radnai, L. et al. Discovery of selective inhibitors for in vitro and in vivo interrogation of Skeletal Myosin II. *ACS Chem. Biol.* **16**, 2164–2173 (2021).
- Dogterom, M. & Koenderink, G. H. Actin-microtubule crosstalk in cell biology. *Nat. Rev. Mol. Cell Biol.* **20**, 38–54 (2019).
- Yu, P., Santiago, L. Y., Katagiri, Y. & Geller, H. M. Myosin II activity regulates neurite outgrowth and guidance in response to chondroitin sulfate proteoglycans. *J. Neurochem.* **120**, 1117–1128 (2012).
- Wang, X. W. et al. Knocking out non-muscle myosin II in retinal ganglion cells promotes long-distance optic nerve regeneration. *Cell Rep.* **31**, 107537 (2020).
- Hur, E. M. et al. Engineering neuronal growth cones to promote axon regeneration over inhibitory molecules. *Proc. Natl. Acad. Sci. USA* **108**, 5057–5062 (2011).
- Varkuti, B. H. et al. A highly soluble, non-phototoxic, non-fluorescent blebbistatin derivative. *Sci. Rep.* **6**, 26141 (2016).
- Young, E. J. et al. Nonmuscle myosin IIB as a therapeutic target for the prevention of relapse to methamphetamine use. *Mol. Psychiatry* **21**, 615–623 (2016).
- MILLER CG, Patrick; KAMENECKA, Theodore; RUMBAUGH, Gavin; SURMAN, Matthew; YOUNG, Steve; DUDDY, Steven; RADNAL, Laszlo, inventorsNONMUSCLE MYOSIN II INHIBITORS FOR SUBSTANCE USE RELAPSE patent WO 2019/241469 A1. 2019 December 10, (2019).
- Klim, J. R. et al. ALS-implicated protein TDP-43 sustains levels of STMN2, a mediator of motor neuron growth and repair. *Nat. Neurosci.* **22**, 167–179 (2019).
- Fournier, A. E., Takizawa, B. T. & Strittmatter, S. M. Rho kinase inhibition enhances axonal regeneration in the injured CNS. *J. Neurosci.* **23**, 1416–1423 (2003).
- Roy, A., Pathak, Z. & Kumar, H. Strategies to neutralize RhoA/ROCK pathway after spinal cord injury. *Exp. Neurol.* **343**, 113794 (2021).

33. Dravid, A., Raos, B., Svirskis, D. & O'Carroll, S. J. Optimised techniques for high-throughput screening of differentiated SH-SY5Y cells and application for neurite outgrowth assays. *Sci Rep.* **11**, 23935 (2021).
34. Verhasselt, S., Roman, B. I., Bracke, M. E. & Stevens, C. V. Improved synthesis and comparative analysis of the tool properties of new and existing D-ring modified (S)-blebbistatin analogs. *Eur. J. Med. Chem.* **136**, 85–103 (2017).
35. Zhang, Z. et al. Automated preclinical detection of mechanical pain hypersensitivity and analgesia. *Pain* **163**, 2326–2336 (2022).
36. Qian, T. et al. The dynamic changes of main cell types in the microenvironment of sciatic nerves following sciatic nerve injury and the influence of let-7 on their distribution. *RSC Adv.* **8**, 41181–41191 (2018).
37. Garrido-Casado, M., Asensio-Juarez, G. & Vicente-Manzanares, M. Nonmuscle myosin II regulation directs its multiple roles in cell migration and division. *Annu. Rev. Cell Dev. Biol.* **37**, 285–310 (2021).
38. Elliott, H. et al. Myosin II controls cellular branching morphogenesis and migration in three dimensions by minimizing cell-surface curvature. *Nat. Cell Biol.* **17**, 137–147 (2015).
39. Hall, A. & Lalli, G. Rho and Ras GTPases in axon growth, guidance, and branching. *Cold Spring Harb. Perspect. Biol.* **2**, a001818 (2010).
40. Da Silva, J. S. et al. RhoA/ROCK regulation of neuritogenesis via profilin IIa-mediated control of actin stability. *J. Cell Biol.* **162**, 1267–1279 (2003).
41. Turney, S. G. & Bridgman, P. C. Laminin stimulates and guides axonal outgrowth via growth cone myosin II activity. *Nat. Neurosci.* **8**, 717–719 (2005).
42. Wilkinson, S., Paterson, H. F. & Marshall, C. J. Cdc42-MRCK and Rho-ROCK signalling cooperate in myosin phosphorylation and cell invasion. *Nat. Cell Biol.* **7**, 255–261 (2005).
43. Kalil, K. & Dent, E. W. Branch management: mechanisms of axon branching in the developing vertebrate CNS. *Nat. Rev. Neurosci.* **15**, 7–18 (2014).
44. Kubow, K. E., Conrad, S. K. & Horwitz, A. R. Matrix microarchitecture and myosin II determine adhesion in 3D matrices. *Curr. Biol.* **23**, 1607–1619 (2013).
45. Marmo, A. C. & Grunlan, M. A. Biomedical Silicones: Leveraging Additive Strategies to Propel Modern Utility. *ACS Macro Lett.* **12**, 172–182 (2023).
46. Yiu, G. & He, Z. Glial inhibition of CNS axon regeneration. *Nat. Rev. Neurosci.* **7**, 617–627 (2006).
47. Oliver, K. M. et al. Molecular correlates of muscle spindle and Golgi tendon organ afferents. *Nat. Commun.* **12**, 1451 (2021).
48. Wu, H. et al. Distinct subtypes of proprioceptive dorsal root ganglion neurons regulate adaptive proprioception in mice. *Nat. Commun.* **12**, 1026 (2021).
49. de Nooij, J. C. & Zampieri, N. The making of a proprioceptor: a tale of two identities. *Trends Neurosci.* **46**, 1083–1094 (2023).
50. Swaminathan, V. & Waterman, C. M. The molecular clutch model for mechanotransduction evolves. *Nat. Cell Biol.* **18**, 459–461 (2016).
51. Tan, C. L. et al. Integrin activation promotes axon growth on inhibitory chondroitin sulfate proteoglycans by enhancing integrin signaling. *J. Neurosci.* **31**, 6289–6295 (2011).
52. Boulting, G. L. et al. A functionally characterized test set of human induced pluripotent stem cells. *Nat. Biotechnol.* **29**, 279–286 (2011).
53. Dalvai, M. et al. A scalable genome-editing-based approach for mapping multiprotein complexes in human cells. *Cell Rep.* **13**, 621–633 (2015).
54. Berryer, M. H. et al. High-content synaptic phenotyping in human cellular models reveals a role for BET proteins in synapse assembly. *Elife.* **12**, <https://doi.org/10.7554/elife.80168> (2023).
55. Schafer, S. T. et al. Pathological priming causes developmental gene network heterochronicity in autistic subject-derived neurons. *Nat. Neurosci.* **22**, 243–255 (2019).
56. Kadoshima, T. et al. Self-organization of axial polarity, inside-out layer pattern, and species-specific progenitor dynamics in human ES cell-derived neocortex. *Proc. Natl. Acad. Sci. USA* **110**, 20284–20289 (2013).
57. Fazzari, E. et al. Glioblastoma neurovascular progenitor orchestrates tumor cell type diversity. Preprint at <https://doi.org/10.1101/2024.07.24.604840> (2024).
58. Winzeler, A. & Wang, J. T. Purification and culture of retinal ganglion cells from rodents. *Cold Spring Harb. Protoc.* **2013**, 643–652 (2013).
59. Renthall, W. et al. Transcriptional reprogramming of distinct peripheral sensory neuron subtypes after axonal injury. *Neuron* **108**, 128–144 (2020).
60. Sleight, J. N., Burgess, R. W., Gillingwater, T. H. & Cader, M. Z. Morphological analysis of neuromuscular junction development and degeneration in rodent lumbrical muscles. *J. Neurosci. Methods* **227**, 159–165 (2014).
61. Mech, A. M., Brown, A. L., Schiavo, G. & Sleight, J. N. Morphological variability is greater at developing than mature mouse neuromuscular junctions. *J. Anat.* **237**, 603–617 (2020).
62. Sleight, J. N., Grice, S. J., Burgess, R. W., Talbot, K. & Cader, M. Z. Neuromuscular junction maturation defects precede impaired lower motor neuron connectivity in Charcot-Marie-Tooth type 2D mice. *Hum. Mol. Genet.* **23**, 2639–2650 (2014).

Acknowledgements

This work was funded by Dr. Miriam and Sheldon G Adelson Medical Research Foundation (H.I.K. and C.J.W.), NIH (R35NS105076, C.J.W.), SMA foundation (C.J.W.), a Leonard and Isabelle Goldenson fellowship (to T.S.-Y.H.) and the Ellen R. and Melvin J. Gordon Center for the Cure and Treatment of Paralysis Award (to K.H. and T.S.-Y.H.). We also thank Yiming Zhang for helping with lentivirus preparation at the viral core at Boston Children's Hospital. We further thank Jennifer Smith and the ICCB-Longwood Screening Facility at Harvard Medical School, Riki Kawaguchi, Daniel H. Geschwind at the University of California Los Angeles, Natalia P. Biscola and Leif A. Havton at Mount Sinai, and Christopher V. Gabel at Boston University for their invaluable contributions and support. Lastly, we thank our colleagues Andrew Snaveley, Bhagat Singh, Yung-Chih Cheng, Laurel Heckman, Long Cheng, Seungeun Oh, Xili Liu and Xuan Huang at Boston Children's Hospital and Harvard Medical School who provided expertise and advice that greatly assisted the research.

Author contributions

Conceptualization, K.H., T.S.-Y.H., Z.H., H.I.K., and C.J.W.; Methodology, K.H., T.S.-Y.H., X.Z., B.L.T., M.A., S.J., K.C., M.C.C., E.F., X.S., J.T.H., Z.X., X.C., A.B., L.B.B., and J.H.; Validation, K.H., T.S.-Y.H., X.Z., B.L.T., K.Z., J.T.H., X.C., G.K., L.P., and R.P.; Formal analysis, K.H., T.S.-Y.H., X.Z., B.L.T., S.J., and M.C.C.; Investigation, K.H., T.S.-Y.H., X.Z., B.L.T., K.C., J.T.H., and M.C.C.; Resources, L.B.B. and C.J.W.; Original draft, K.H., T.S.-Y.H., and C.J.W.; Supervision, Z.H., H.I.K., and C.J.W.

Competing interests

C.J.W. is a founder of Nocion Therapeutics, QurAlis, and BlackBox Bio and is on the scientific advisory board of Lundbeck Pharma, Axonis, and Tafalgie Therapeutics. Z.H. is a co-founder of Rugen and Myrobalan, and an advisor of Axonis. The remaining authors declare no competing interests.

Additional information

Supplementary information The online version contains supplementary material available at <https://doi.org/10.1038/s41467-025-58303-6>.

Correspondence and requests for materials should be addressed to Clifford J. Woolf.

Peer review information *Nature Communications* thanks Melissa Andrews and the other anonymous reviewer(s) for their contribution to the peer review of this work. A peer review file is available.

Reprints and permissions information is available at <http://www.nature.com/reprints>

Publisher's note Springer Nature remains neutral with regard to jurisdictional claims in published maps and institutional affiliations.

Open Access This article is licensed under a Creative Commons Attribution-NonCommercial-NoDerivatives 4.0 International License, which permits any non-commercial use, sharing, distribution and reproduction in any medium or format, as long as you give appropriate credit to the original author(s) and the source, provide a link to the Creative Commons licence, and indicate if you modified the licensed material. You do not have permission under this licence to share adapted material derived from this article or parts of it. The images or other third party material in this article are included in the article's Creative Commons licence, unless indicated otherwise in a credit line to the material. If material is not included in the article's Creative Commons licence and your intended use is not permitted by statutory regulation or exceeds the permitted use, you will need to obtain permission directly from the copyright holder. To view a copy of this licence, visit <http://creativecommons.org/licenses/by-nc-nd/4.0/>.

© The Author(s) 2025